Fluctuation statistics in the scrape-off layer of Alcator C-Mod

R. Kube,* A. Theodorsen, and O.E. Garcia

Department of Physics and Technology,

UiT - The Arctic University of Norway, N-9037 Tromsø, Norway

B. LaBombard and J.L. Terry

MIT Plasma Science and Fusion Center, Cambridge, MA, 02139, USA

(Dated: February 15, 2016)

Abstract

We study long time series of the ion saturation current and floating potential, sampled by Langmuir probes dwelled in the outboard mid-plane scrape off layer and embedded in the lower divertor baffle of Alcator C-Mod. A series of ohmically heated L-mode plasma discharges is investigated with line-averaged plasma density ranging from $\overline{n}_e/n_G = 0.15$ to 0.42, where n_G is the Greenwald density. All ion saturation current time series that are sampled in the far scrape-off layer are characterized by large-amplitude burst events. Coefficients of skewness and excess kurtosis of the time series obey a quadratic relationship and their histograms coincide partially upon proper normalization. Histograms of the ion saturation current time series are found to agree well with a prediction of a stochastic model for the particle density fluctuations in scrape-off layer plasmas.

The distribution of the waiting times between successive large-amplitude burst events and of the burst amplitudes are approximately described by exponential distributions. The average waiting time and burst amplitude are found to vary weakly with the line-averaged plasma density. Conditional averaging reveals that the radial blob velocity, estimated from floating potential measurements, increases with the normalized burst amplitude in the outboard mid-plane scrape-off layer. For low density discharges, the conditionally averaged waveform of the floating potential associated with large amplitude bursts at the divertor probes has a dipolar shape. In detached divertor conditions the average waveform is random, indicating electrical disconnection of blobs from the sheaths at the divertor targets.

I. INTRODUCTION

The far scrape-off layer of magnetically confined plasmas is dominated by intermittent fluctuations of the particle density and concomitant large transport events. A large body of research links these phenomena to the radial propagation of plasma filaments which are elongated along the magnetic field and localized in the radial-poloidal plane. [1–9]. They carry excess particle density and heat relative to the background plasma and are hence called *blobs* Blobs are believed to mediate the parallel and perpendicular transport channels of particle and heat fluxes in the scrape-off layer. Furthermore may blob propagation be responsible for a significant heat load on plasma facing components of the vacuum vessel. As the empirical discharge density limit [10] is approached, the relative magnitude of these transport channels changes such as to favor perpendicular transport [11 and 12]. To understand the impact of blobby transport on plasma confinement, their mode of propagation as well as the statistics of fluctuation induced transport have to be studied.

The basic mechanism underlying plasma blob propagation is the interchange mechanism. [2, 13–17]. Magnetic gradient and curvature drifts in an inhomogeneous magnetic field give rise to an electric current which polarizes filament structures of elevated pressure perpendicular to the magnetic field and its direction of variation. At the outboard mid-plane location of a toroidally magnetized plasma, a filament of elevated pressure is polarized in such a way that it propagates radially outwards towards the main chamber wall [2].

The path along which electric currents within the filament are closed are crucial for its radial velocity. Assuming that the electric current in the plasma filament can flow freely along magnetic field lines within the plasma filament, the electric current loop may be closed through these sheaths. Two-dimensional fluid simulations of isolated plasma blob propagation reveal that the radial blob velocity decreases with increasing magnitude of the parallel electric currents, parameterized by a sheath dissipation parameter [2, 16, and 17]. Sheath connection is expected to be limited by ballooning of the plasma filaments and large plasma resistivity which prevents parallel electric currents through the sheaths [18–21]. Fluid modeling of plasma blobs furthermore reveals a dependence of its radial velocity, v_{rad}, on the relative blob amplitude, where blobs with larger amplitude feature a larger radial center of mass velocity [22–24].

Studies of plasma blob propagation in Alcator C-Mod show a good agreement between

their radial velocity and the sheath-connected velocity scaling law when the scrape-off layer is sheath-limited [24]. Work at Alcator C-Mod furthermore reveals correlation coefficients of up to 75% between time series of particle density proxies, sampled at different poloidal positions along a single magnetic field line [25 and 26]. This supports the idea that blobs in Alcator C-Mod may extend from the outboard mid-plane to the divertor sheaths and are sheath connected in suitable low-density plasmas.

The turbulent flows in the far scrape-off layer of magnetically confined plasmas have been demonstrated to have many universal properties [27–31]. For one, the conditionally averaged waveform of large amplitude events in particle density time series presents a fast rise and a slow fall [4–6, 32–39]. The conditionally averaged waveform as well as the histogram of ion saturation current time series were found to collapse upon normalization for a range of line-averaged plasma densities and plasma currents in the *Tokamak à configuration variable* (TCV) tokamak [8, 36, and 38]. Exponentially distributed burst amplitudes and waiting times have been observed in the scrape-off layer of Alcator C-Mod and TCV [39 and 48]. Correlation analysis further reveals the presence of a dipolar electric potential structure centered around local maxima of the particle density [25, 40–42].

Time series with frequent large amplitude bursts feature histograms with elevated tails as well as positive coefficients of sample skewness and excess kurtosis [27, 30, 43, and 44]. The universal character of the fluctuations manifests itself in the fact that histograms of the particle density coincide upon normalization when obtained at a single position in the far scrape-off layer for various plasma parameters [27, 29, 30, 38, and 44]. Particle density fluctuations in the scrape-off layer sampled at the TCV device were also found to be well described by a Gamma and a log-normal distribution over a large range of discharge parameters [30].

Another salient feature of the density time series is a quadratic relation between sample skewness, S, and excess kurtosis, F, of the form $F = a + bS^2$, where a and b are real coefficients [30, 45, and 46]. This relation is intrinsic to some probability distribution functions that have been proposed to describe histograms of the particle density time series. Data sampled in the TORPEX device over a large range of discharge conditions and spatial locations was shown to be well described by the generalized beta distribution [46]. Recent work models particle density time series as a stochastic process which is based on the superposition of individual pulses [47]. Under the assumption that the individual pulses decay

3

exponentially, have exponentially distributed amplitudes and waiting times between pulses, this model predicts the particle density time series to be Gamma distributed. It was shown that this model describes the intensity fluctuations at the outboard mid-plane scrape-off layer of Alcator C-Mod, as measured by gas-puff imaging, over several decades in normalized probability [48]. So far however, no consensus on one particular analytic model exists in the fusion community.

In this paper, we present an analysis of long time series of the ion saturation current and floating potential obtained by Langmuir probes in the boundary region of the Alcator C-Mod tokamak. Utilizing a probe dwelled in the outboard mid-plane scrape-off layer as well as probes embedded in the divertor baffle allows us to study the universality of the fluctuations sampled at these two positions as well as the dependence of the statistics on the line-averaged plasma density.

The structure of this article is as follows. Section II introduces a stochastic model for density fluctuations in the scrape-off layer as well as the conditional averaging method to be used. The experimental setup is described in Section III. Section IV presents the time series analysis data sampled by the probe in the outboard mid-plane scrape-off layer and Section V presents the corresponding analysis of the time series obtained from the divertor probes. A discussion of the universal properties of the time series sampled in both positions and their relation to blob theory are given in Section VI. We conclude in Section VII with suggestions for further work.

II. FLUCTUATION STATISTICS

Recent work models the particle density fluctuations at a single point in scrape-off layer plasmas as the superposition of random pulse events [47]:

$$\Phi(t) = \sum_k A_k \phi(t - t_k). \tag{1}$$

Given that the arrival of pulses in the time series is governed by a Poisson process, this model predicts a quadratic relation between coefficients of skewness and excess kurtosis. Moreover, by assuming a Poisson distribution it follows that the waiting time between pulses are exponentially distributed. Further assuming an exponential pulse shape, $\phi(t) = \Theta(t) \exp(-t/\tau_{\mathrm{d}})$, where Θ is the Heaviside step function and τ_{d} the duration time of a pulse,

and exponentially distributed pulse amplitudes A_k, the model implies that the particle density is Gamma distributed [47]. The ratio of pulse duration time and waiting times, $\gamma = \tau_\mathrm{d}/\tau_\mathrm{w}$, is the shape parameter of the Gamma distribution.

To include random fluctuations of the background particle density we add normal distributed noise to the signal Eqn. (1),

$$\Phi'(t) = \Phi(t) + N(t). \tag{2}$$

Here the normal distributed noise N has vanishing mean and variance σ^2. The resulting probability density function of the random variable is then given by the convolution of a Γ-distribution and a normal distribution and can be written using two parameters: γ and ϵ. While γ relates to the ratio of pulse decay and waiting time as before, in other words the density of pulse arrivals, ϵ relates the variance of N to the root mean square value of Φ via $\sigma^2 = \epsilon \Phi_\mathrm{rms}^2$. A large value of ϵ denotes the case where the root mean square value of the process Φ is smaller than the scale parameter of the white noise N and a small value of ϵ denotes the converse relation.

It is commonly observed in particle density fluctuation time series in scrape-off layer plasmas that pulses overlap as to form large amplitude burst events. To determine the average structure of the bursts we employ conditional averaging [49]. Starting from the largest burst event in the time series at hand, we identify a set of disjunct sub records, placed symmetrically around the peak of burst events which exceed a given amplitude threshold until no more burst events exceeding this threshold are left uncovered. The threshold is often chosen to be 2.5 times the root mean square value of the time series at hand. This average can be written as

$$C(\tau) = \langle \Phi(\tau) | \Phi(\tau = 0) > 2.5\,\Phi_\mathrm{rms} \rangle, \tag{3}$$

where τ is the time offset relative to the peak of the burst. The variability of the burst events is characterized by the conditional variance [50]:

$$1 - \mathrm{CV}(\tau) = 1 - \frac{\langle (\Phi - C)^2 | \Phi(0) > 2.5\,\Phi_\mathrm{rms} \rangle}{C^2}. \tag{4}$$

This quantity is bounded, $0 < 1 - \mathrm{CV}(\tau) < 1$, where the values 0 and 1 indicate respectively no and perfect reproducibility of the conditionally averaged waveform.

To study the intermittency of ion saturation current time series, they are rescaled according to

$$\widetilde{I} = \frac{I - \overline{I}_{\mathrm{mv}}}{I_{\mathrm{rms,mv}}}. \tag{5}$$

The subscripts mv and rms, mv denote the moving average and moving root mean square value respectively. Both are computed within a window of 16384 elements when applied to data from the horizontal scanning probe. This window corresponds to roughly 3ms and exceeds typical autocorrelation times of approximately $15\,\mu$s by a factor of 200 [11]. The same window length is used for the time series obtained by the divertor probes. In the latter case, this corresponds to approximately $20\,$ms. Since the amplitude of the density fluctuation in the scrape-off layer is sensitive to the distance to the last closed flux surface we compute the statistics within a moving window as to alleviate the fluctuations of the last closed flux surface indicated in Fig. 4. The use of such averaging has little influence on the conditional averaging threshold Eqn. (3). Time series of the floating potential are rescaled by removing a linear trend from the time series and subsequently normalizing the time series to the electron temperature and as to have vanishing mean:

$$\widetilde{V} = \frac{e\left(V - \overline{V}\right)}{T_{\mathrm{e}}}. \tag{6}$$

We do not use a moving average for the floating potential since the amplitude of the signal varies little with distance to the last closed flux surface.

III. EXPERIMENTAL SETUP

Alcator C-Mod is a compact tokamak with a major radius of $R = 0.68\,$m and a minor radius of $a = 0.22\,$m, and allows for a magnetic field of up to 8T on-axis. Figure 1 shows a cross-section of Alcator C-Mod together with the diagnostics from which we report measurements: the horizontal and vertical scanning probes and the Langmuir probe array embedded in the lower outer divertor baffle. The magnetic equilibrium from discharge 2 of Tab. I, as reconstructed by EFIT [51], is overlaid. The Mach probe head installed on both scanning probes, depicted in Fig. 2, is designed to routinely withstand heat fluxes of up to $100\,\mathrm{MW/m}^2$ [52 and 53]. All electrodes are connected to sampling electronics that sample current and voltage with $5\,$MHz and 14 bit resolution. The horizontal scanning probe is

installed 10 cm above the outboard mid-plane and can be reciprocated horizontally 11 cm into the plasma. For the present experiments this probe was dwelled at a fixed position in the scrape-off layer for the entire duration of the plasma discharge. As a common radial coordinate we employ the magnetic flux label ρ, which gives the distance to the last-closed flux surface (LCFS) as mapped to the outboard mid-plane along magnetic field lines. This coordinate is calculated by magnetic equilibrium reconstruction with the EFIT code using input from a set of magnetic diagnostics installed in the vacuum vessel [54]. For positions in the near and far scrape-off layer, the probe was targeted to dwell at $\rho \approx 3\,\mathrm{mm}$ and at $\rho \approx 8\,\mathrm{mm}$ respectively. The north-east (NE) and south-east (SE) electrodes were biased to $-290\,\mathrm{V}$ with respect to the vacuum vessel in order to sample the ion saturation current. The south-west (SW) and north-west (NW) electrodes were electrically floating. This allows to estimate the poloidal electric field from these electrodes as

$$E \approx \frac{V^{\mathrm{SW}} - V^{\mathrm{NW}}}{\triangle_{\mathrm{p}}}, \tag{7}$$

where $\triangle_{\mathrm{p}} = 2.24\,\mathrm{mm}$ is the poloidal separation between the electrodes. The vertical scanning probe was set up to plunge through the scrape-off layer up to the last closed flux surface, as depicted by the vertical line in Fig. 1, three times per plasma discharge. A triangular voltage waveform, sweeping from $-255V$ to $55\,\mathrm{V}$ with a frequency of $2\,\mathrm{kHz}$ was applied to all four electrodes of the probe head. The electron temperature T_{e} is obtained by fitting a three parameter exponential function on the measured voltage-current characteristic of each probe head with a spatial resolution of $\triangle_{\rho} = 1\,\mathrm{mm}$ [55].

The Langmuir probe array embedded in the lower divertor baffle consists of two electrodes per probe which were configured to sample the ion saturation current and floating potential respectively with $0.4\,\mathrm{MHz}$ with 16 bit resolution. In the targeted magnetic equilibrium configuration the two outermost divertor probes map to $\rho \approx 8 - 10\,\mathrm{mm}$. This corresponds to the approximate position where the horizontal scanning probe was dwelled in the far scrape-off layer within error margins of $5\,\mathrm{mm}$.

We report from measurements obtained in 5 ohmically heated plasmas in a lower single null magnetic geometry with $5.4\,\mathrm{T}$ on-axis magnetic field and a plasma current of $I_{\mathrm{p}} = 0.6\,\mathrm{MA}$. For all discharges it was attempted to minimize the movement of the strike point of the last closed flux surface on the lower divertor baffle. As a consequence, the estimated position of the last closed flux surface at the outboard mid-plane is subject to

larger fluctuations. Table I lists the plasma parameters of all shots as well as the position of the horizontal scanning probe, the time interval on which the time series are analyzed, and the plot marker used in the following figures. The electron temperature at $\rho = 5$mm which is used to normalize the floating potential and to estimate the acoustic velocity at the position of the horizontal scanning probe is also listed. In discharge 1 the horizontal scanning probe was dwelled in the near scrape-off layer, this data is not directly comparable to the far scrape-off layer data. In discharge 3 the sensitivity of the electronics of the divertor probes was not adjusted correctly such that this data is not analyzed either. Radial profiles of the electron temperature are shown in Fig. 3.

The upper panel of Fig. 4 shows the time traces of the line-averaged particle density for the analyzed discharges. The middle panel shows the radial coordinate of the probe head of the horizontal scanning probe and the lower panel shows the radial coordinates of the two outermost divertor probes. While the line-averaged plasma density is approximately constant and the radial coordinate of the divertor probes show a slight drift, the radial coordinate of the horizontal scanning probe is subject to larger fluctuations. The indicated time intervals in this figure correspond to the interval of the time series used for data analysis. These time intervals are chosen such as to keep the line-averaged particle density of any given discharge within $\triangle_{\overline{n}_e/n_G} \approx 0.02$ and the radial position of the horizontal scanning probe within an interval of $\triangle_\rho \approx 5$mm of the reference position.

Discharge	$\overline{n}_e/n_G$	T_e/eV	Probe position	t_{start}/s	t_{end}/s	Plot marker
1	0.15	35	near SOL	0.75 (0.75)	1.10 (1.10)	▼
2	0.28	25	far SOL	0.65 (0.65)	1.50 (1.50)	◆
3	0.32	25	far SOL	0.80 (–)	1.10 (–)	■
4	0.31	20	far SOL	0.80 (0.80)	1.10 (1.10)	●
5	0.42	20	far SOL	0.50 (0.50)	0.70 (0.70)	▲

TABLE I. List of the plasma parameters and the time interval used for time series analysis. The numbers in parenthesis give the interval on which data from the divertor probe is used. A dash indicates that no data is available.

IV.   OUTBOARD MID-PLANE PLASMA FLUCTUATIONS

We begin by analyzing the time series sampled by the horizontal scanning probe in the near scrape-off layer. This is discharge 1 in tab. I with $\overline{n}_e/n_G = 0.15$. The histogram of the normalized time series, shown in Fig. 5, is almost gaussian and the time series, shown in the inset of the figure, appears to be random. With a mean value of $\overline{I} = 6.1 \times 10^{-2}$A and a root mean square value given by $I_{rms} = 1.4 \times 10^{-2}$ the relative fluctuation level of the time series is $I_{rms}/\overline{I} = 0.22$. Coefficients of skewness and excess kurtosis are given by $S = 0.27$ and $F = -0.07$ respectively. A best fit on the model Eqn. (2) yields $\gamma = 30$ and $\epsilon = 6.24 \times 10^{-6}$. This describes a process with mostly gaussian statistics, as suggested by the histogram and the statistics of the time series.

We continue by analyzing the time series sampled by the horizontal scanning probe in the far scrape-off layer. Figure 6 shows the histogram of the ion saturation current, normalized according to Eqn. (5), as sampled by the north-east electrode of the horizontal scanning probe during discharge 2 with $\overline{n}_e/n_G = 0.28$. The length of the time series is $0.85\,\mathrm{s}$ and its histogram spans over four decades in normalized probability. It presents an elevated tail with fluctuations exceeding six times the root mean square of the time series. The raw time series prominently features positive, large amplitude bursts events. The histogram of data sampled by the south-east electrode is quantitatively similar. A sample mean of $\overline{I} = 4.0 \times 10^{-2}\,\mathrm{A}$ and $I_{rms} = 1.3 \times 10^{-2}\,\mathrm{A}$, yields a normalized fluctuation level of $I_{rms}/\overline{I} = 0.32$. Sample coefficients of skewness and excess kurtosis are given by $S = 0.78$ and $F = 0.96$. A non-linear least squares fit on the model described by Eqn. (2) yields $\gamma = 6.35$ and $\epsilon = 2.6 \times 10^{-5}$. This describes the situation where the fluctuation level of the background fluctuations is well below the fluctuation level introduced by the bursts in the time series.

Figure 7 shows the histogram of the normalized ion saturation current time series sampled during discharge 5 with $\overline{n}_e/n_G = 0.42$. The histogram presents an elevated tail with fluctuations well exceeding six times the root mean square of the time series. The mean of the time series is given by $\overline{I} = 9.4 \times 10^{-2}$A and its root mean square value is given by $I_{rms} = 4.6 \times 10^{-2}$A. This yields a normalized fluctuation level of $I_{rms}/\overline{I} = 0.49$, coefficients of skewness and excess kurtosis are given by $S = 1.5$ and $F = 3.5$. The time series presents positive, large amplitude burst events, which seem to occur less frequent as in Fig. 6. The best fit on the model given by Eqn. (2) yields $\gamma = 1.06$ and $\epsilon = 1.85 \times 10^{-1}$, suggesting that

background fluctuations are of larger relative magnitude than in the previous case.

Figure 8 shows the conditionally averaged waveforms and their conditional variance of the normalized data time series sampled during discharge 2 with $\overline{n}_{\mathrm{e}}/n_{\mathrm{G}} = 0.28$. The upper row shows the conditionally averaged waveform of large-amplitude bursts occurring in the ion saturation current, as measured by the north-east and south-east electrodes, as well as their conditional variance. The averaged waveform is asymmetric. The best fit of an exponential waveform on the rise and fall give an e-folding rise time of $\tau_{\mathrm{r}} \approx 2\,\mu\mathrm{s}$ and fall time of $\tau_{\mathrm{f}} \approx 4\,\mu\mathrm{s}$ respectively. Their reproducibility is close to unity within the interval centered around $\tau = 0\,\mu\mathrm{s}$, bounded by the e-folding times, and it shows the same asymmetry as the burst shape.

The conditionally averaged floating potential waveform, computed by setting the trigger condition on bursts in the ion saturation current time series as sampled by the north-east electrode, is shown in the middle row of Fig. 8. The south-west electrode measures a dipolar waveform where the positive peak is sampled before the negative peak. The peak-to-valley range of the waveform is approximately 0.3 where the positive peak is larger in absolute value than the negative peak by a factor of 2. The waveform sampled by the north-west electrode is more symmetric, and features a peak-to-valley range of approximately 0.2. The positive peak is also more reproducible with $1 - \mathrm{CV} \approx 0.3$ compared to $1 - \mathrm{CV} \approx 0.2$ for the north-west electrode.

Rather triggering on the south-east electrode, the conditionally averaged floating potential waveforms are also dipolar with peak-to-valley ranges of approximately $0.2\,(0.4)$ for the south-west (north-west) electrode. The reproducibility of the waveform is larger by a factor of two for the latter. Opposite to the situation where the trigger is on the north-east electrode, here the reproducibility is larger on the north-west electrode where the negative part of the blobs electric potential dipole is measured after its density maximum has traversed the probe.

Such poloidal motion is in agreement with the picture of a dipolar electric potential structure, centered around the particle density maximum of a plasma blob which is moving into the direction of $\boldsymbol{B} \times \nabla B$, i.e. poloidally downwards. This is compatible with measurements using gas-puff imaging [56 and 58]. For the plasma blob to propagate radially outwards, the negative pole of the electric potential has to be poloidally above the particle density maximum and the positive pole has to be poloidally below the particle density maximum. When

10

the particle density maximum is recorded by the north-east electrode, the positive pole of the potential structure has traversed the south-west electrode. This explains the pronounced positive pole for $\tau < 0$ of the south-west electrode and its relatively large reproducibility. The negative pole of the potential structure traverses the north-west electrode for $\tau > 0$ and leads to a large reproducibility of the waveform.

The conditionally averaged waveform of the estimated poloidal electric field is a monopolar structure with a peak value of approximately $-2500\,\mathrm{Vm^{-1}}(-3000\,\mathrm{Vm^{-1}})$ when triggered on bursts occurring on the north-east (south-east) electrode. Using that the toroidal magnetic field at the probe position is approximately $4.0\,\mathrm{T}$, this corresponds to a local average electric drift velocity of $v_{\mathrm{rad}} \approx 600 - 700\,\mathrm{ms^{-1}}$. Radial blob velocities of similar magnitude have been reported from gas-puff imaging measurements [24 and 58].

We continue by elucidating the relation between the amplitudes of the bursts and their associated radial velocity. For this, we approximate the time it takes for a blob to traverse the probe by $\tau_{\mathrm{r}} + \tau_{\mathrm{f}}$. Both e-folding times are found by a least squares fit of an exponential function on the rise and fall of the conditionally averaged burst shape respectively. The electric drift velocity associated with a burst event is then computed using the estimated poloidal electric field averaged over the interval $[-\tau_{\mathrm{r}} : \tau_{\mathrm{f}}]$.

Figure 9 shows the radial electric drift velocity associated with burst events in the ion saturation current on the north east electrode plotted against its normalized amplitude. The radial velocities rarely exceed 5% of the ion acoustic velocity. Approximately 90% of all events have a velocity directed towards the main chamber wall and the Pearson sample correlation coefficient increases from $r = 0.19$ for $\overline{n}_{\mathrm{e}}/n_{\mathrm{G}} = 0.28$ (left panel, 5253 events), to $r = 0.29$ for $\overline{n}_{\mathrm{e}}/n_{\mathrm{G}} = 0.31$ (middle panel, 1203 events), to $r = 0.36$ for $\overline{n}_{\mathrm{e}}/n_{\mathrm{G}} = 0.42$ (right panel, 833 events). To guide the eye on the sample correlation, a green straight line, denoting a linear fit on the value pairs, has been over plotted in all scatter plots.

Conditional averaging further reveals the distribution of waiting times between successive large amplitude burst events and of the burst amplitudes of the normalized time series at hand. For discharges where multiple electrodes sample the ion saturation current, only data sampled by the north east electrode is used.

The shape of the sampled histograms indicates that the waiting times and the burst amplitudes are approximately described by an exponential distribution. The description by the exponential model appears more accurate for the waiting times than for the burst

amplitudes. For an exponentially distributed random variable $X > 0$, the complementary cumulative distribution function is given by

$$1 - F_X(X) = \exp\left(-\frac{X - X_0}{\langle X \rangle}\right). \tag{8}$$

Here F_X is the cumulative distribution function, $\langle X \rangle$ is the scale parameter of the distribution, in the cases discussed here the average waiting time and average burst amplitude, and X_0 is the location parameter of the distribution. To obtain the average waiting time of the distribution from sampled data we employ a maximum likelihood estimate. This method is unbiased in the sense that all data points are equally weighted when estimating the scale parameter [59]. The location parameter is given by the conditional averaging sub record length in the case of waiting time distributions and the conditional averaging threshold in the case of burst amplitude distributions.

Figure 10 shows the histograms of the sampled waiting times between successive burst events with amplitudes exceeding 2.5. Compared are best fits on Eqn. (8), denoted by full lines. The exponential model gives a good description of the waiting times over more than one decade in normalized probability for all discharges. The average waiting time is between $\langle \tau_{\mathrm{w}} \rangle \approx 0.12\,\mathrm{ms}$ for $\overline{n}_{\mathrm{e}}/n_{\mathrm{G}} = 0.28$, $0.20\,\mathrm{ms}$ and $0.26\,\mathrm{ms}$ for discharges 3 and 4, and $0.18\,\mathrm{ms}$ for discharge 5 where $\overline{n}_{\mathrm{e}}/n_{\mathrm{G}} = 0.42$. No trend between the line-averaged plasma density and the average waiting time is observed.

Histograms of the sampled normalized burst amplitudes are compared to the best fits of Eqn. (8) in Fig. 11. We find that the burst amplitude histograms are approximately described by an exponential distribution over approximately one decade. However, as all time series feature significant pulse overlap, the burst amplitude histogram is only suggestive of the actual amplitude distribution of the individual pulses that make up the signal. The average burst value is between $\langle A \rangle = 1.1$ for $\overline{n}_{\mathrm{e}}/n_{\mathrm{G}} = 0.28$ and $\langle A \rangle = 1.3$ for $\overline{n}_{\mathrm{e}}/n_{\mathrm{G}} = 0.42$, with no apparent correlation to the line-averaged density. That is, the average burst amplitude is approximately given by the root mean square value of the time series.

V. DIVERTOR PLASMA FLUCTUATIONS

We proceed by analyzing data time series sampled by the Langmuir probes embedded in the lower divertor in the same manner as in the previous section. Figure 12 presents

the histogram of the normalized ion saturation current time series for discharge 1 with $\overline{n}_{\mathrm{e}}/n_{\mathrm{G}} = 0.15$, as sampled by the two outermost divertor probes 9 (shown in the upper panel) and 10 (shown in the lower panel). The average current at probe 9 is $\overline{I} = 4.4 \times 10^{-2}$A and the root mean square value is given by $I_{\mathrm{rms}} = 1.5 \times 10^{-2}$A, which yields a relative fluctuation level of $I_{\mathrm{rms}}/\overline{I} = 0.33$. As shown in the upper panel of Fig. 12, the sample presents only slightly elevated tails, fluctuations in the time series rarely exceed four times the root mean square value of the time series. Coefficients of skewness and excess kurtosis are given by $S = 0.41$ and $F = -0.28$. The histogram of the ion saturation current as sampled by divertor probe 10 presents a more elevated tail with fluctuations exceeding five times the root mean square value of the time series. With $\overline{I} = 2.9 \times 10^{-2}$A and $I_{\mathrm{rms}} = 9.0 \times 10^{-3}$A the relative fluctuation level is $I_{\mathrm{rms}}/\overline{I} = 0.31$. The best fit on the model Eqn. (2) yields $\gamma = 9.9\,(5.8)$ and $\epsilon = 2.0 \times 10^{-5}\,(7.3 \times 10^{-4})$ for the time series sampled by probe 9 (10).

Figure 13 presents the histograms of the normalized ion saturation current time series sampled by the divertor probes for discharge 5 with $\overline{n}_{\mathrm{e}}/n_{\mathrm{G}} = 0.42$. Both time series present fluctuations of up to five times the sample root mean square value. For the time series obtained by probe 9 the sample mean is given by $\overline{I} = 0.20\,\mathrm{A}$ and the root mean square value is given by $I_{\mathrm{rms}} = 7.8 \times 10^{-2}\,\mathrm{A}$. This gives a normalized fluctuation level of $I_{\mathrm{rms}}/\overline{I} = 0.38$. Sample coefficients of skewness and excess kurtosis are given by $S = 1.3$ and $F = 2.3$, which reflects the non-gaussian character of the fluctuations. Continuing with the histogram of the normalized ion saturation current time series sampled by probe 10, shown in the lower panel of Fig. 13, we find its histogram to be similar to the histogram sampled by probe 9. The ion saturation current fluctuation amplitudes do not exceed six times the sample root mean square value. Values of the sample mean, root-mean square and relative fluctuation level are given by $\overline{I} = 0.20$A, $I_{\mathrm{rms}} = 5.7 \times 10^{-2}$A, and $I_{\mathrm{rms}}/\overline{I} = 0.28$, coefficients of sample skewness and excess kurtosis are given by $S = 1.0$ and $F = 1.8$. The best fit on the model described by Eqn. (2) yields $\gamma = 2.2\,(1.4)$ and $\epsilon = 5.3 \times 10^{-2}\,(3.5 \times 10^{-1})$ for the time series sampled by probe 9(10).

We continue by analyzing the conditionally averaged waveforms of the time series sampled by probe 10. For discharge 5 with $\overline{n}_{\mathrm{e}}/n_{\mathrm{G}} = 0.42$ we assume a detached divertor and use half the electron temperature measured by the vertical scanning probe, $T_{\mathrm{e}} = 10\,\mathrm{eV}$, to normalize the floating potential time series [60]. Fig. 14 shows the conditionally averaged waveforms for discharges 1 ($\overline{n}_{\mathrm{e}}/n_{\mathrm{G}} = 0.15$), 2 ($\overline{n}_{\mathrm{e}}/n_{\mathrm{G}} = 0.28$), and 5 ($\overline{n}_{\mathrm{e}}/n_{\mathrm{G}} = 0.42$). For discharges 1

and 2 the conditionally averaged burst shape is nearly symmetric. Least squares fits of an exponential function on the burst shape yield e-folding times of $\tau_r \approx 12\,\mu\mathrm{s}$ and $\tau_f \approx 14\,\mu\mathrm{s}$ and $\tau_r \approx 14\,\mu\mathrm{s}$ and $\tau_f \approx 12\,\mu\mathrm{s}$ respectively. The conditionally averaged burst shape for discharge 5 is asymmetric with a rise time of $\tau_r \approx 26\,\mu\mathrm{s}$ and a fall time of $\tau_f \approx 66\mu\mathrm{s}$. All conditionally averaged burst shapes are highly reproducible.

The conditionally averaged waveform of the floating potential is shown in the lower panel of Fig. 14. For discharges 1 and 2 the conditionally averaged floating potential waveforms associated with large amplitude bursts in the ion saturation current have a dipolar shape with a pronounced positive peak and are reproducible. For discharge 5 the conditionally averaged waveform is irregular, showing only a weak positive peak, and is irreproducible.

We continue by studying the intermittency of large amplitude burst events in the normalized ion saturation current time series sampled by divertor probe 10. Figure 15 shows histograms of the waiting times between successive large amplitude burst events in the time series. Full lines denote Eqn. (8) with an average waiting time obtained by a maximum likelihood estimate and a location parameter given by $\tau_{w,0} = 0.1\,\mathrm{ms}$. All histograms are well approximated by an exponential distribution over one decade in probability. Average waiting times between large amplitude burst events are between $0.28\,\mathrm{ms}$ and $0.43\,\mathrm{ms}$, approximately twice as large as observed in time series sampled in the outboard mid-plane scrape-off layer. Figure 16 shows the histogram of the burst amplitudes in the time series. Maximum likelihood estimates of the average burst amplitude are $\langle A \rangle \approx 0.6$ for $\overline{n}_e/n_G = 0.15$ and 0.30, which increases to $\langle A \rangle \approx 0.9$ for $\overline{n}_e/n_G = 0.42$. As in the case of the horizontal scanning probe data, no systematic variation of the scale length with line-averaged particle density is observable. The average burst amplitude is approximately half the amplitude found for the time series sampled in the outboard mid plane scrape-off layer.

VI.   DISCUSSION

Long ion saturation current time series, with sample lengths between 0.2 and $0.85\,\mathrm{s}$ have been sampled in the outboard mid-plane scrape-off layer and at the outer divertorr, during discharges with line averaged plasma densities ranging from $\overline{n}_e/n_G = 0.15$ to $\overline{n}_e/n_G = 0.42$. A statistical analysis shows that the time series in the far scrape-off layer are characterized by large relative fluctuation levels and intermittent large-amplitude burst events. The sample

14

Shot	$\overline{n}_{\mathrm{e}}/n_{\mathrm{G}}$	$I_{\mathrm{rms}}/\overline{I}$	S	F
1	0.15	0.22* / 0.33 / 0.33	0.27* / 0.41 / 0.41	0.07* / −0.28 / −0.29
2	0.28	0.32 / 0.35 / 0.31	0.78 / 0.71 / 0.55	0.96 / 0.53 / 7.5×10^{-3}
3	0.32	0.34 / − / −	1.2 / − / −	2.2 / − / −
4	0.31	0.33 / 0.40 / 0.37	1.1 / 0.98 / 0.87	1.9 / 1.3 / 0.81
5	0.42	0.49 / 0.39 / 0.28	1.5 / 1.3 / 1.0	3.5 / 2.3 / 1.8

TABLE II. Statistics of the entire time series sampled by the horizontal scanning probe / divertor probe 9 / divertor probe 10. The values marked with a * are sampled in the near scrape-off layer and are not directly comparable to the other values.

statistics of all ion saturation current time series discussed in this paper are collected in Tab. II. The data sampled in the near scrape-off layer presents Gaussian statistics, consistent with previous measurements in the near scrape-off layer [11]. In the outboard midplane far scrape-off layer we find that the relative fluctuation level increases gradually from 0.32 for discharge 2 ($\overline{n}_{\mathrm{e}}/n_{\mathrm{G}} = 0.28$) to 0.49 in discharge 5 ($\overline{n}_{\mathrm{e}}/n_{\mathrm{G}} = 0.42$). A similar increase is found for divertor probe 9, where $I_{\mathrm{rms}}/\overline{I}$ increases from 0.33 for $\overline{n}_{\mathrm{e}}/n_{\mathrm{G}} = 0.15$, over 0.35 for $\overline{n}_{\mathrm{e}}/n_{\mathrm{G}} = 0.28$ to 0.39 for $\overline{n}_{\mathrm{e}}/n_{\mathrm{G}} = 0.42$. On the other hand, the relative fluctuation level of the time series sampled by divertor probe 10 shows no significant change as the line-averaged density is changed between discharges. Sample coefficients of skewness and excess kurtosis are found to increase in all time series as the line-averaged density increases. Thus, the intermittency level increases with the line-averaged density in these ohmic plasmas.

Figure 17 shows the sample skewness plotted against the sample excess kurtosis, computed for time series sub records of 20ms, sampled in the outboard midplane far scrape-off layer during discharges 2 – 4. Both S and F increase with $\overline{n}_{\mathrm{e}}/n_{\mathrm{G}}$. A least squares fit of the model $F = a + bS^2$ on the value pairs yields $a = -0.20 \pm 0.04$ and $b = 1.51 \pm 0.03$. The relation between sample coefficients of skewness and excess kurtosis of the time series sampled by the divertor probes, shown in Fig. 18, is qualitatively similar to those from the horizontal scanning probe. The sample coefficients have a smaller range and notably feature small, feature negative values of excess kurtosis. A least squares fit on the quadratic model yields $a = -0.50 \pm 0.02$ and $b = 1.78 \pm 0.03$. The fit parameters have similar magnitude as found for the outboard mid-plane far scrape-off layer. The clustering of the sample pairs

is also similar to the clustering for the horizontal scanning probe data. Samples taken in low line-average density discharges present smaller coefficients than samples taken in high line-averaged density discharges, implying that time series from higher density discharges are more intermittent.

The values of sample skewness and excess kurtosis for the outboard mid-plane time series fall in a range between $0.0 \leq S \leq 2.0$ and $0.0 \leq F \leq 6.0$. These ranges are considerably lower than observed for a similar analysis of gas-puff imaging data in Alcator C-Mod [48]. In the latter case, the view of the diagnostics includes the area of the wall shadow, characterized by a considerably lower plasma background density. As plasma blobs propagate into this region, they are registered in the intensity time series as amplitudes which are significantly larger than the background intensity signal. This leads to large values of sample skewness and excess kurtosis.

Histograms of time series sampled in the outboard mid-plane far scrape-off layer present elevated tails with fluctuations exceeding six times the root mean square value of the time series. The time series sampled by the divertor probes show qualitatively the same features, albeit with a lower normalized fluctuation magnitude. Figures 19 and 20 show histograms of the ion saturation current and floating potential time series, normalized according to Eqs. (5) and (6), sampled in all discharges listed in Tab. I. The ion saturation current histograms do not collapse perfectly but may be separated by where they are sampled. Histograms sampled in the far scrape-off layer present consistently slightly more elevated tails than histograms sampled in the divertor region. Within each group, the highest density discharges feature the histograms with the most elevated tails. The floating potential histograms are approximately normal distributed. The time series sampled in the out board mid-plane scrape-off layer show a slightly elevated tail compared to a normal distribution in positive and negative abscissa regions while the time series sampled in the divertor region show an elevated tail in negative abscissa regions and a lowered tail in positive abscissa regions.

The distribution of waiting times between large-amplitude bursts in ion saturation current time series is found to be well described by an exponential distribution for both, time series sampled in the outboard mid plane scrape-off layer as well and in the divertor region. This suggests that the individual large amplitude pulses are uncorrelated and that their occurrence is governed by a Poisson process. It is exactly this property for which the stochastic model of Ref. [47] predicts a quadratic relation between skewness and excess

16

Shot	$\overline{n}_\mathrm{e}/n_\mathrm{G}$	$\langle A \rangle$	$\langle \tau_\mathrm{w} \rangle$
1	0.15	$-$ / 0.37 / 0.27	$-$ / 0.37 / 0.64
2	0.28	0.12 / 0.26 / 0.38	1.1 / 0.61 / 0.49
3	0.32	0.20 / $-$ / $-$	1.2 / $-$ / $-$
4	0.31	0.26 / 0.37 / 0.43	1.2 / 0.66 / 0.64
5	0.42	0.28 / 0.37 / 0.38	1.3 / 0.98 / 0.91

TABLE III. Average amplitude and waiting times between conditionally averaged events compared for time series sampled by the horizontal scanning probe / divertor probe 9 / divertor probe 10.

kurtosis.

The histograms of the normalized burst amplitudes, Fig. 11 and Fig. 16, are furthermore compatible with the assumption the pulse amplitudes are exponentially distributed. The evidence for this is however less clear than for the waiting times, mostly because the exponential model given by Eqn. (8) is only a good fit in the uppermost decade. This is due to the fixed location parameter and the conservation of probability limiting the choices of the slope of the cumulative distribution function. The estimated shape parameter of the stochastic model Eqn. (2) is $1 \lesssim \gamma \lesssim 10$ for all distributions sampled in the far scrape-off layer. This described the low intermittency case, i.e. pulses arrive frequently and overlap as to form large amplitude burst events. As a consequence the amplitudes taken from the bursts in the time series overestimate the underlying pulse amplitudes. This is reflected in the curved shape of the histograms Figs. 11 and 16. However, the presented maximum likelihood estimates agree well with the complementary cumulative distribution function over approximately one decade.

Conditional averaging of the ion saturation current time series further reveals an average burst shape that features a steep rise and a slow fall, both of which are well described by an exponential waveform. Typical rise times and fall times of the events in the time series sampled by the horizontal scanning probe are given by $\tau_\mathrm{r} \approx 5\,\mu\mathrm{s}$ and $\tau_\mathrm{f} \approx 10\,\mu\mathrm{s}$, while the corresponding values for the time series sampled by the divertor probes are larger by a factor of 2. We note however that the time resolution of the divertor probes is $2.5\,\mu\mathrm{s}$ which might affect the accuracy of the e-folding times negatively. The conditionally averaged structure of the time series sampled by divertor probe 10 in discharge 5 shows a larger asymmetry

17

with a large fall time. However, the waveforms sampled by the divertor probes do not allow to draw conclusions about the physical dimensions of impinging plasma filaments. The recorded waveform may be due to both, a filament traversing the probe radially outwards or a filament impinging along the direction of the magnetic field on to the probe.

The conditionally averaged waveforms of the normalized ion saturation current and the floating potential signal, sampled at the outboard mid-plane far scrape-off layer, support the conventional picture of plasma blob propagation through the scrape-off layer. That is, peaks in the plasma particle density are associated with a dipolar electric potential structure whose polarization gives an electric drift velocity pointing towards the vessel wall. The phase shift between the conditionally averaged waveforms of the ion saturation current and floating potential is approximately $\pi/2$ and the estimated radial velocities of the blobs structure are in the order of a few per cent of the ion acoustic velocity for all line averaged plasma densities. These results extend previous measurements made in the scrape off layer of Alcator C-Mod [25]. A positive linear correlation is observed between the estimated radial blob velocities and their normalized amplitude, with Pearson sample correlation coefficients given by 0.19 for $\overline{n}_e/n_G = 0.28$ and 0.36 for $\overline{n}_e/n_G = 0.42$. A possible explanation for this correlation is that the pressure gradient within the blob structure increases with filament amplitude. Fluid modeling of isolated plasma filaments shows that the magnitude of the plasma pressure gradient increases the plasma vorticity associated with the plasma blob [16]. Assuming that the poloidal size of the plasma blobs is constant [24], this creates a larger electric field which in turn increases the electric drift magnitude.

A simple estimate of parallel and perpendicular transport for a filament, see for example Fig. 3 in [36], suggests that the bursts in the time series sampled by the divertor probes may be due to plasma filaments impinging in the probes. For this we note that potential variations may also be caused by the internal temperature profile of plasma blobs [61]. For $T_e = 30\,\text{eV}$ we evaluate the electron thermal velocity to be $v_{\text{th,e}} \approx 2 \times 10^6\,\text{ms}^{-1}$ and the ion acoustic velocity in a deuterium plasma to be $C_s = \sqrt{T_e/m_i} \approx 4 \times 10^4\,\text{ms}^{-1}$. A lower bound on the characteristic velocity associated with transport of potential perturbations along the magnetic field is given by $v_{\text{th,e}}$ [26]. Given a connection length of $L_\| \approx 10\,\text{m}$, the particles and potential generated by a blob ballooned on the low-field side will reach the divertor targets after $\tau_{\text{n},\|} \approx 3 \times 10^{-4}\,\text{s}$ and $\tau_{\text{e},\|} \approx 4 \times 10^{-6}\,\text{s}$ respectively. Assuming that the blob is instantiated as a structure with sharp modulation along a flux tube and that it

18

propagates normal to the flux tube at $v_{\text{rad}} = 500\,\text{ms}^{-1}$, independent of poloidal angle, the time estimate above implies that the footprint of the blob has reached the divertor sheaths at radial coordinates given by $\rho_{\text{E}} \approx 2 \times 10^{-3}\,\text{m}$ and $\rho_{\text{n}} \approx 1 \times 10^{-1}\text{m}$. This interpretation is compatible with previous results from correlation analysis of particle density proxies along single field lines in Alcator C-Mod and NSTX [25, 26, and 57].

Neglecting electron temperature fluctuations, a dipolar potential structure measured by the divertor probes may be interpreted as the footprint of a plasma blob. When this is the case, the radial velocity scaling of the plasma filaments falls in the sheath connected regime. On the other hand, a random waveform implies that the electric current loop within a plasma filament closes upstream of the divertor. On the other hand, random structures have been observed in numerical simulations of plasma blobs where the late blob has dispersed by Rayleigh-Taylor and Kelvin-Helmholtz instabilities [16] and in three-dimensional simulations, where no coherent structure of the late blob is recognizable [20].

The hypothesis that the blobs are not electrically connected to the sheaths in discharge 5 is however also compatible with measurements of radial blob velocities in high density plasmas in Alcator C-Mod, which indicate that the radial filament velocity at the outboard mid-plane increases with increasing line-averaged density and exceed the value predicted for sheath connected blobs [24 and 58].

This hypothesis is further supported by histograms of the radial particle flux in the outboard mid-plane far scrape-off layer, shown in Fig. 21. Upon proper normalization, the histograms for discharges 2, 3, and 4 collapse, while the histogram for discharge 5 features a more elevated tail. All histograms feature exponential tails for both the positive and the negative abscissa. The average radial particle flux increases by a factor of approximately 8 from the discharge with $\overline{n}_{\text{e}}/n_{\text{G}} = 0.28$ to the discharge with $\overline{n}_{\text{e}}/n_{\text{G}} = 0.42$. This increase of the radial particle flux with line-averaged plasma density is consistent with previous experiments in the Alcator C-Mod tokamak [11 and 62] as well as with experiments performcd in the TCV tokamak [12]. The higher frequency of large flux events is consistent with the observation that blobs are moving faster while their cross-field size diameter remains constant [24]. Another possible explanation for the high average radial particle flux in discharge 5 may be increased levels of temperature fluctuations due to plasma filaments.

The effective convective velocity, $v_{\text{eff}} = \overline{\Gamma}/\overline{n_{\text{e}}} = \widetilde{I}(\widetilde{V^{\text{SW}} - V^{\text{NW}}})/B\triangle_{\text{p}}$, also increases with the line-averaged plasma density. For discharge 2 we find $v_{\text{eff}} = 57\text{ms}^{-1}$, while we find

$v_{\mathrm{eff}} = 1.1 \times 10^2 \mathrm{ms}^{-1}$ for discharge 3 and 4. For discharge 5 with $\overline{n}_{\mathrm{e}}/n_{\mathrm{G}} = 0.42$ we find $v_{\mathrm{eff}} = 1.5 \times 10^2 \mathrm{ms}^{-1}$.

Such an increase in effective convective velocity is consistent with flux measurements done in the Alcator C-Mod tokamak [11]. The values we find for v_{eff} are furthermore in the same order of magnitude as measured in the Tore Supra Device [63] and in TCV [12].

VII.   CONCLUSION

To conclude, we have studied the dependence of fluctuations in scrape-off layer plasmas on the line-averaged particle density, as measured by Langmuir probes at the outboard mid-plane location and embedded in the outer divertor of Alcator C-Mod. Time series of ion saturation current, sampled in the far-scrape off layer, all feature dynamics which is governed by the intermittent arrival of large amplitude burst events. Waiting times between large amplitude burst events are well described by an exponential distribution. Sub records of the time series feature a quadratic relation between coefficients of sample skewness and sample excess kurtosis. The fact that large-amplitude events occur uncorrelated and the quadratic relation between sample skewness and excess kurtosis, support assumptions of a stochastic model for the density fluctuations in scrape-off layer plasmas. The probability density function of this model describes the histograms of all sampled ion saturation current time series well.

The conditionally averaged waveform of the associated potential fluctuations is dipolar, except for time series sampled in the divertor plasma where the divertor is detached. This supports the hypothesis that plasma blobs are electrically detached in sufficiently high density plasmas and may explain the observed increase in radial blob velocity with line-averaged plasma density [24 and 58]. Electric disconnection of the plasma blobs from the divertor sheaths may also explain recent experiments performed at the ASDEX Upgrade tokamak where it was observed that the radial blob velocity and cross-field diameter increases as the divertor detaches [64].

Future work will include a more detailed comparison of the stochastic model to time series measured in scrape-off layer plasmas. Work on a manuscript providing a detailed discussion of the stochastic model presented in this article is in progress.

VIII. ACKNOWLEDGEMENTS
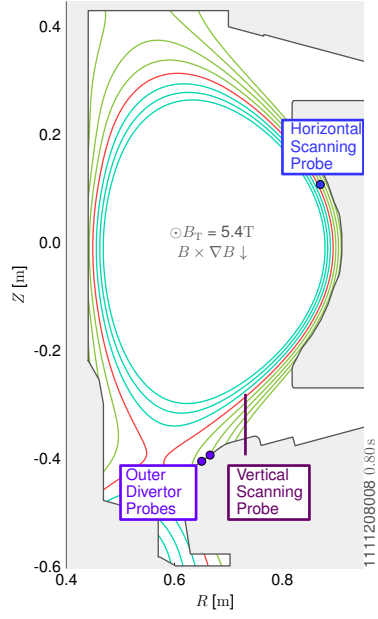
FIG. 1. Cross-section of Alcator C-Mod showing the diagnostics from which we report measurements: The horizontal scanning probes as well as two probes of the outer divertor probe array. Overlaid are magnetic field lines from discharge 2, as reconstructed by EFIT.

Scanning Probe Electrode Geometry
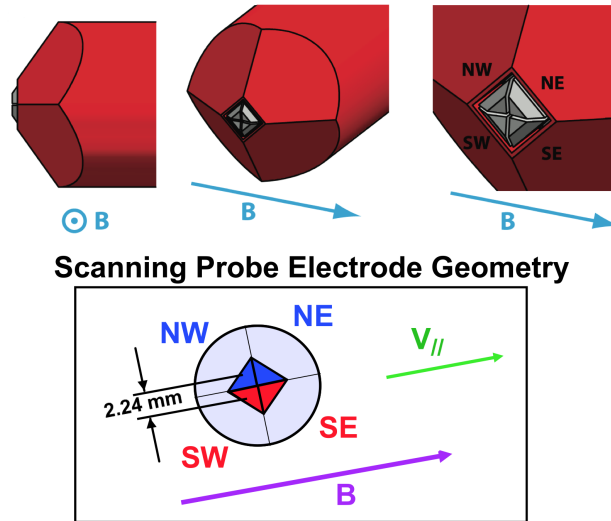
FIG. 2. Mach probe head installed on the horizontal and vertical scanning probes.
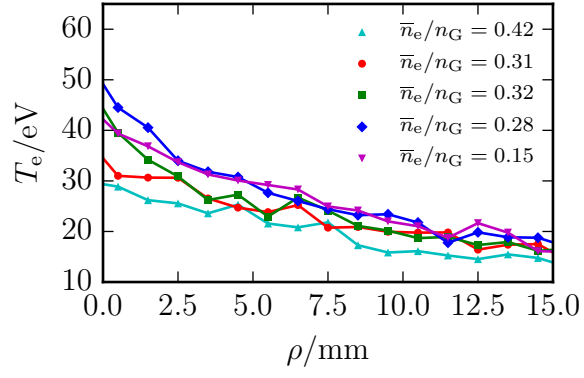
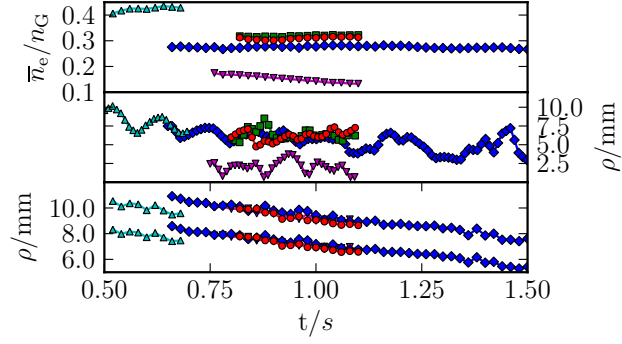FIG. 3. Radial profiles of the electron temperature as measured by the vertical scanning probe.

FIG. 4. Evolution of the line-averaged particle density (upper panel) and radial coordinate for the horizontal scanning probe (mid panel). An offset of $\rho_0 = 5\,\text{mm}$ has been added to the position of the horizontal scanning probe. The lower panel shows the radial coordinate for the two outer most divertor probes. Table I lists the used plot markers.

25
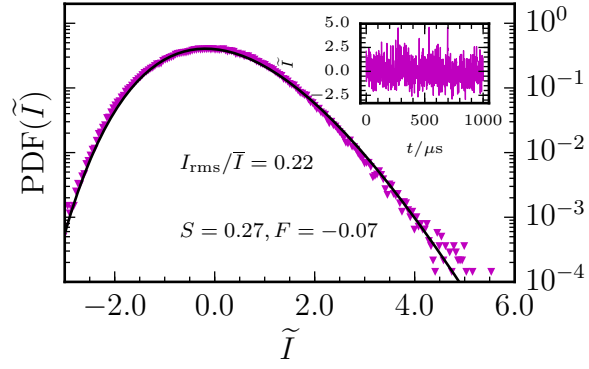
FIG. 5. Histogram of the normalized ion saturation current as sampled by the north-east electrode of the horizontal scanning probe dwelled in the near scrape-off layer during discharge 1 with $\overline{n}_{\mathrm{e}}/n_{\mathrm{G}} = 0.15$. The black line indicates the best fit of the stochastic model on the histogram and the inset shows a 1ms long sub record of the normalized ion saturation current time series.
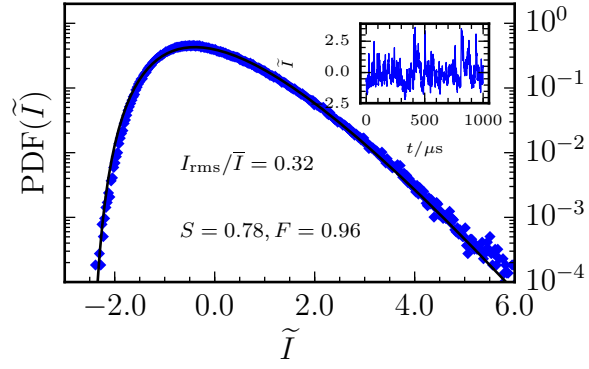
FIG. 6. Histogram of the normalized ion saturation current as sampled by the north-east electrode of the horizontal scanning probe dwelled in the far scrape-off layer during discharge 2 with $\overline{n}_{\mathrm{e}}/n_{\mathrm{G}} = 0.28$. The black line indicates the best fit of the stochastic model on the histogram and the inset shows a 1ms long sub record of the normalized ion saturation current time series.
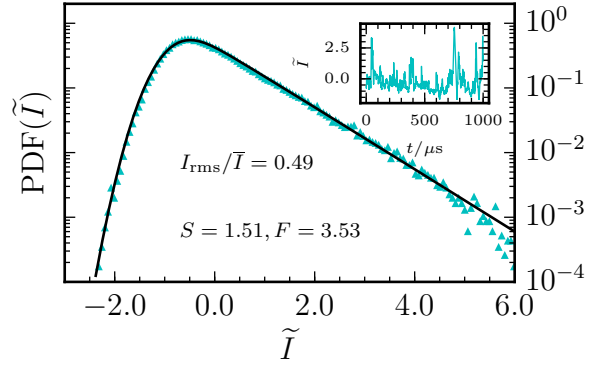
FIG. 7. Histogram of the normalized ion saturation current as sampled by the north-east electrode of the horizontal scanning probe dwelled in the far scrape-off layer during discharge 5 with $\overline{n}_{\mathrm{e}}/n_{\mathrm{G}} = 0.42$. The black line indicates the best fit of the stochastic model on the histogram and the inset shows a 1ms long sub record of the normalized ion saturation current time series.
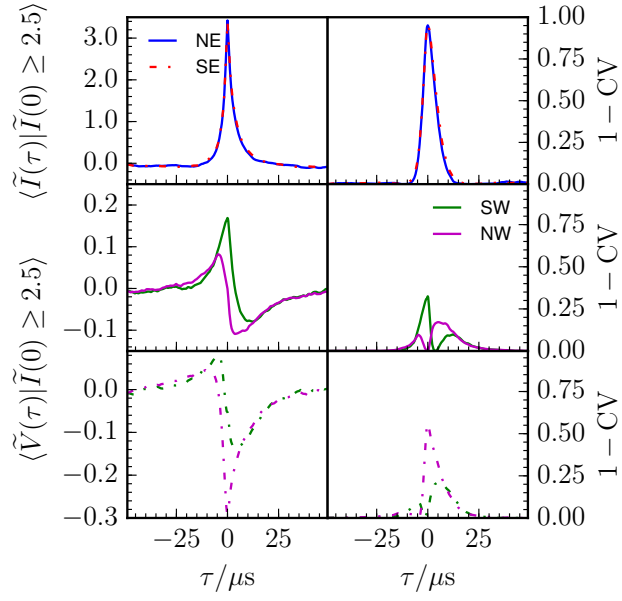
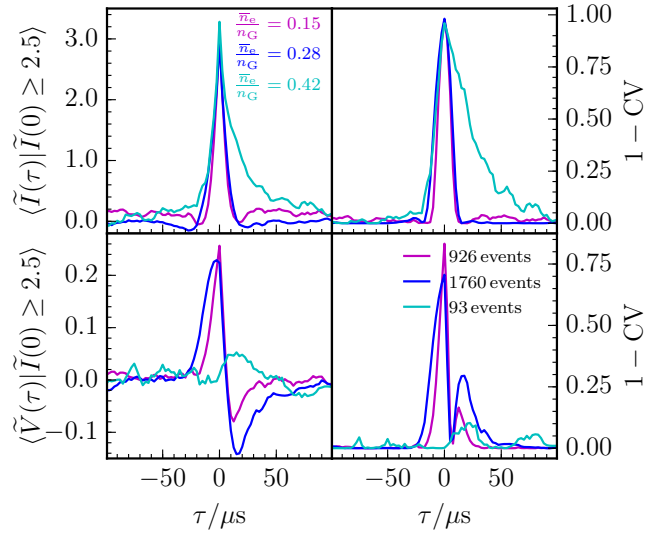FIG. 8. Conditionally averaged burst shape and conditional variance for the ion saturation current (upper row), floating potential when triggered by bursts on the north-east electrode (middle row), and floating potential when triggered by bursts on the south-east electrode (bottom row) for discharge 2 with $\overline{n}_\mathrm{e}/n_\mathrm{G} = 0.28$.
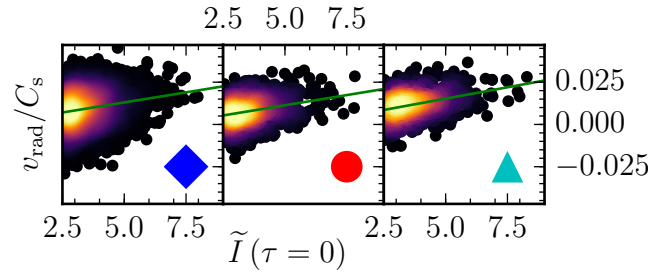
FIG. 9. Estimated radial velocity as a function of normalized burst amplitude with the best fit of a linear function denoted by the green line. The data is sampled by the horizontal scanning probe dwelling in the far scrape-off layer and the plot marker refers to Tab. I.
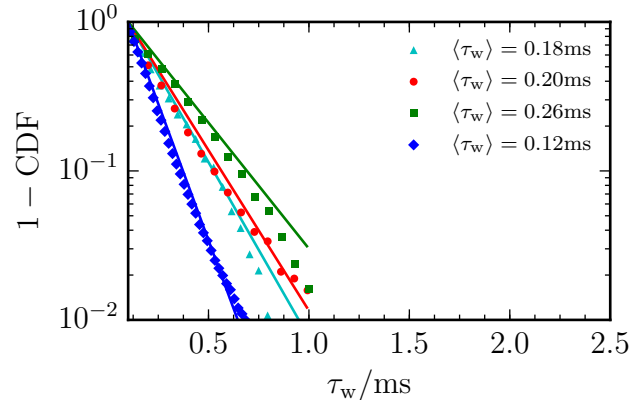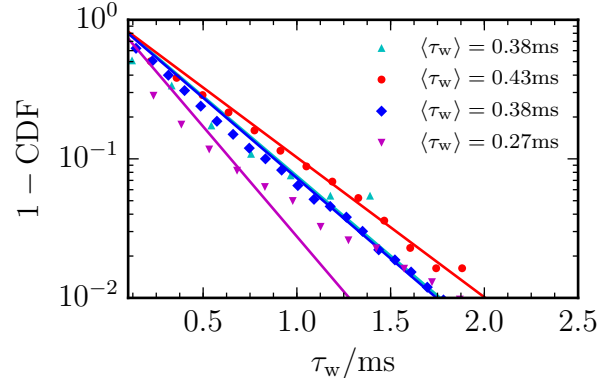
FIG. 10. Distribution of waiting times between successive large amplitude burst events in the normalized ion saturation current time series as measured by the horizontal scanning probe in the far scrape-off layer. The plot markers refer to discharges listed in Tab. I.
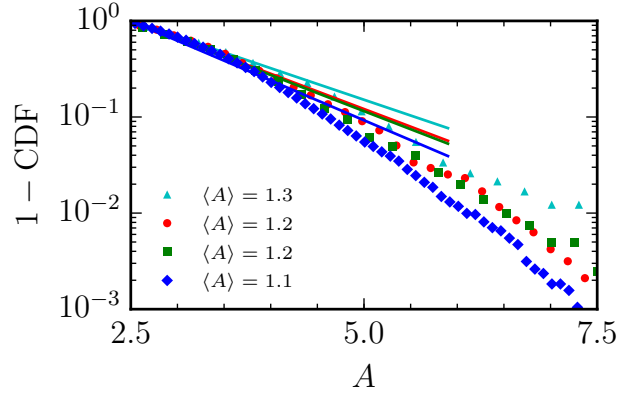
FIG. 11. Amplitude distribution of burst events in the normalized ion saturation current time series as measured by the horizontal scanning probe in the far scrape-off layer. The plot markers refer to shots as described in Tab. I.
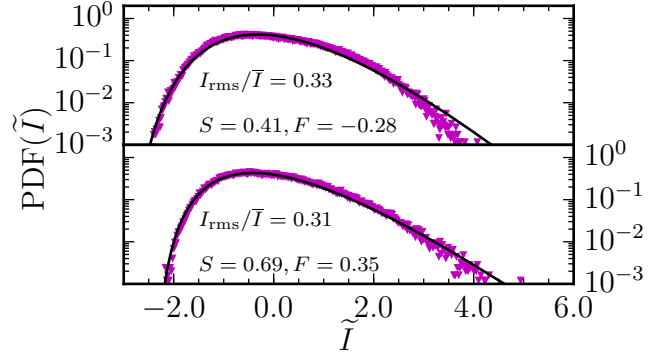
FIG. 12. Histogram of the normalized ion saturation current as sampled by divertor probes 9 (upper panel), and 10 (lower panel) for discharge 1 with $\overline{n}_\mathrm{e}/n_\mathrm{G} = 0.15$. Compared is a fit on the stochastic model Eqn. (2).
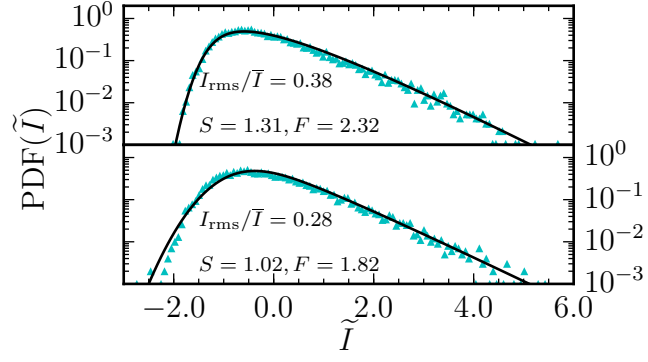
FIG. 13. Histogram of the normalized ion saturation current as sampled by divertor probes 9 (upper panel), and 10 (lower panel) for discharge 5 with $\overline{n}_{\mathrm{e}}/n_{\mathrm{G}} = 0.42$. Compared is a fit on the stochastic model Eqn. (2).

FIG. 14. Conditionally averaged burst shape and conditional variance for the normalized ion saturation current (upper row) and floating potential structure with conditional variance (bottom row) as measured by divertor probe 10.

FIG. 15. Distribution of waiting times between successive large amplitude burst events in the normalized ion saturation current time series as measured by the outermost divertor probe.
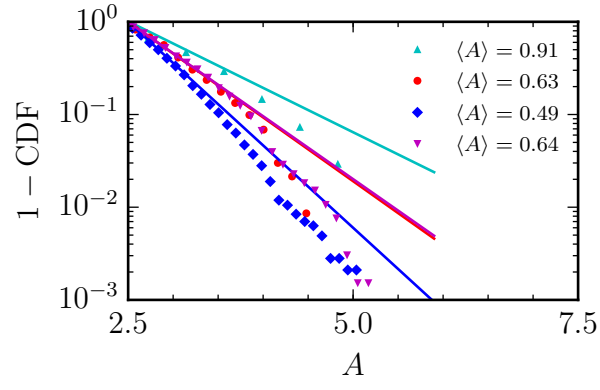
FIG. 16. Amplitude distribution of burst events in the ion saturation current time series as measured by the outermost divertor probe.
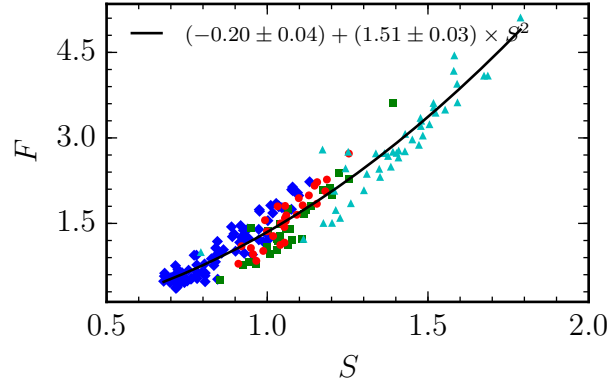
FIG. 17. Coefficients of skewness and excess kurtosis computed for 20ms long sub samples of the ion saturation current as sampled by the horizontal scanning probe.
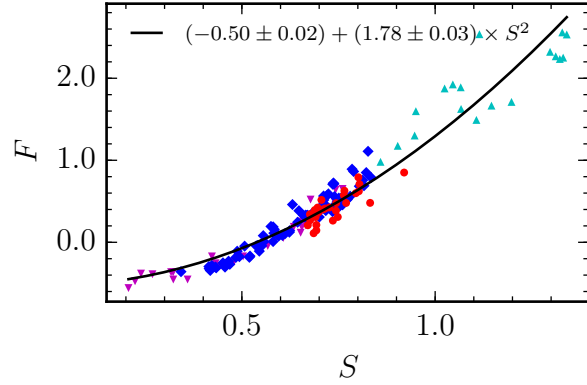

FIG. 18. Coefficients of skewness and excess kurtosis computed for 20ms long sub samples of the ion saturation current as sampled by the outermost divertor probe.
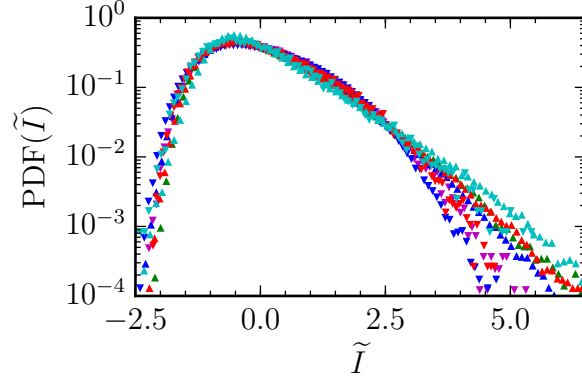
FIG. 19. Rescaled histogram of all sampled ion saturation current time series, normalized according to Eqn. (5). Color coding of the plot markers is as in Tab. I, triangle up denotes data sampled at outboard mid-plane, triangle down denotes data sampled by the outermost divertor probe.
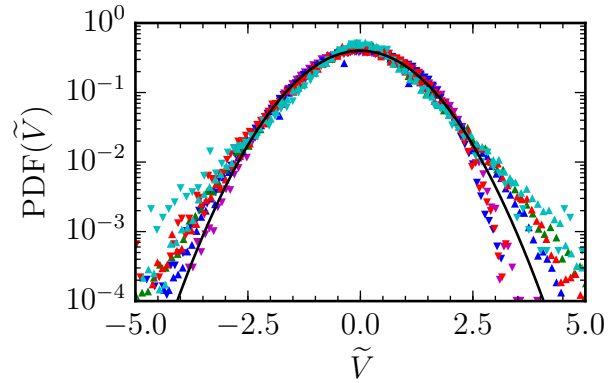

FIG. 20. Rescaled histogram of all sampled floating potential time series, normalized according to Eqn. (6). Color coding of the plot markers is as in Tab. I, triangle up denotes data sampled at outboard mid-plane, triangle down denotes data sampled by the outermost divertor probe.
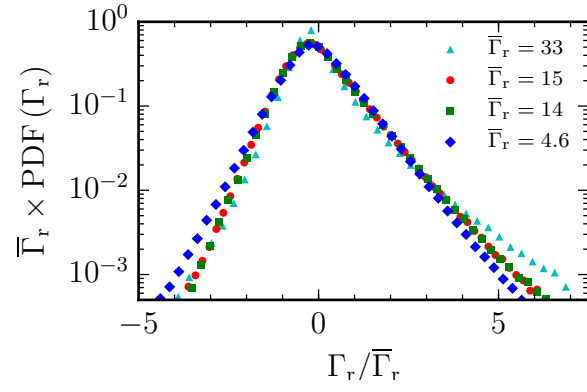
FIG. 21. Rescaled histogram of the radial particle flux as sampled by the horizontal scanning probe. The particle flux is in units of $10^{21}\mathrm{m}^{-2}\mathrm{s}^{-1}$.

* E-mail:ralph.kube@uit.no

[1] A.J. Wootton, B.A. Carreras, H. Matsumoto, K. McGuire, W A. Peebles, Ch.P. Ritz, P W. Terry and S.J. Zweben, Phys. Fluids B **12** 2879-2903 (1990).

[2] S.I. Krasheninnikov, Phys. Lett. A **283** 368 (2001)

[3] S.J. Zweben, R.J. Maqueda, D.P. Stotler, A. Keesee, J. Boedo, C.E. Bush. S.M. Kaye, B. LeBlanc, J.L. Lowrance, V.J. Mastrocola, R. Maingi, N. Nishino, G. Renda, D.W. Swain, J.B. Wilgen and the NSTX Team, Nucl. Fusion **44** 134 (2002)

[4] J.A. Boedo, D.L. Rudakov, R.A. Moyer, S.I. Krasheninnikov, D.G. Whyte, G.R. McKee, G.R. Tynan, M.J. Schaffer, P.C. Stangeby, W.P. West, S. Allen, T.E. Evans, R. Fonck, E. Hollmann, A.W. Leonard, M.A. Mahdavi, G.D. Porter, M. Tillack and G. Antar, Phys. Plasmas **8** 4826 (2001)

[5] J.A. Boedo, D.L. Rudakov, R.A. Moyer, G.R. McKee, R.J. Colchin, M.J. Schaffer, P.C. Stangeby and W.P. West, S.L. Allen, T.E. Evans, R.J. Fonck, E.M. Hollmann, S.I. Krasheninnikov, A.W. Leonard, W. Nevins, M.A. Mahdavi, G.D. Porter, G.R. Tynan, D.G. Whyte and X. Xu, Phys. Plasmas **10** 1670 (2003)

[6] D.L. Rudakov, J.A. Boedo, R.A. Moyer, P.C. Stangeby, J.G. Watkins, D.G. Whyte, L. Zeng, N.H. Brooks, R.P. Doerner, T.E. Evans, M.E. Fenstermacher, M. Groth, E.M. Hollmann, S.I. Krasheninnikov, C.J. Lasnier, A.W. Leonard, M.A. Mahdavi, G.R. McKee, A.G. McLean, A.Yu. Pigarov, W.R. Wampler, G. Wang, W.P. West and C.P.C. Wong, Nucl. Fusion **45** 1589 (2005)

[7] S.J. Zweben, J.A. Boedo, O. Grulke, C. Hidalgo, B. LaBombard, R.J. Maqueda, P. Scarin and J.L. Terry, Plasma Phys. Control. Fusion **49** 51 (2007)

[8] O.E. Garcia, Plasma Fus. Research **4** 19 (2009)

[9] D.A. D'Ippolito, J.R. Myra and S.J. Zweben, Phys. Plasmas **18** 060501 (2011)

[10] M. Greenwald, J.L. Terry, S.M. Wolfe, S. Ejima, M.G. Bell, S.M. Kaye and G.H. Neilson, Nucl. Fusion **28** 2199 (1988)

[11] B. LaBombard, R.L. Boivin, M. Greenwald, J. Hughes, B. Lipschultz, D. Mossessian, C.S. Pitcher, J.L. Terry, S.J. Zweben and the Alcator C-Mod Group, Phys. Plasmas **8** 2107 (2001)

[12] O.E. Garcia, R.A. Pitts, J. Horacek, A.H. Nielsen, W. Fundamenski, J.P. Graves, V. Naulin, J. Juul Rasmussen, J. Nucl. Mater. **363-265** 575 (2007)

41

[13] N. Bian, S. Benkadda, J.V. Paulsen, and O.E. Garcia, Phys. Plasmas **10** 671 (2003)

[14] O.E. Garcia, N.H. Bian, V. Naulin, A.H. Nielsen, and J. Juul Rasmussen, Phys. Scr. **T122** 104 (2006)

[15] C. Theiler, I. Furno, P. Ricci, A. Fasoli, B. Labit, S.H. Müller and G. Plyushchev, Phys. Rev. Lett. **103** 065001 (2009)

[16] O.E. Garcia, N.H. Bian and W. Fundamenski, Phys. Plasmas **13** 082309 (2006)

[17] R. Kube and O.E. Garcia, Phys. Plasmas **18** 102314 (2011)

[18] J.R. Myra, D.A. Russell and D.A. D'Ippolito, Phys. Plasmas **13** 112502 (2006)

[19] D.A. Russell, J.R. Myra and D.A. D'Ippolito, Phys. Plasmas **14** 102307 (2007)

[20] L. Easy, F. Militello, J. Omotani, B. Dudson, E. Havlickova, P. Tamain, V. Naulin and A.H. Nielsen, Phys. Plasmas **21** 122515 (2014)

[21] L. Easy, F. Militello, J. Omotani, N. R. Walkden, and B. Dudson, Phys. Plasmas **23** 012512 (2016)

[22] M. Wiesenberger, J. Madsen, and A. Kendl, Phys. Plasmas **21** 092301 (2014)

[23] J. Angus and S.I. Krasheninnikov, Phys. Plasmas **21** 112504 (2014)

[24] R. Kube, O.E. Garcia, B. LaBombard, J.L. Terry and S.J. Zweben, J. Nucl. Mater. **S438** S505 (2013)

[25] O. Grulke, J.L. Terry, B. LaBombard and S.J. Zweben, Phys. Plasmas **13** 012306 (2006)

[26] O. Grulke, J.L. Terry, I. Cziegler, B. LaBombard and O.E. Garcia, Nucl. Fusion **54** 043012 (2014)

[27] G.Y. Antar, P. Devynck, X. Garbet and S.C. Luckhardt, Phys. Plasmas **8** 1612 (2001)

[28] G.Y. Antar, G. Counsell, Y. Yu, B. LaBombard and P. Devynck, Phys. Plasmas **10** 419 (2003)

[29] B. Ph. van Milligen, R. and Sánchez, B.A. Carreras, V.E. Lynch, B. LaBombard, M.A. Pedrosa, C. Hidalgo, B. Gonçalves, R. Balbín and The W7-AS Team, Phys. Plasmas **12** 052507 (2005)

[30] J.P. Graves, J. Horacek, R.A. Pitts and K.I. Hopcraft, Plasma Phys. Control. Fusion **47** L1 (2005)

[31] J. Horacek, R.A. Pitts and J.P. Graves, Czech Journ. Physics **55** 271 (2005)

[32] D.L. Rudakov, J.A. Boedo, R.A. Moyer, S.I. Krasheninnikov, A.W. Leonard, M.A. Mahdavi, G.R. McKee, G.D. Porter, P.C. Stangeby, J.G. Watkins, W.P. West, D.G. Whyte and G. Antar, Plasma Phys. Control. Fusion **44** 717 (2002)

33 G.S. Kirnev, V.P. Budaev, S.A. Grashin, E.V. Gerasimov and L.N. Khimchenko, Plasma Phys. Control. Fusion **46** 621 (3004)

34 Y.H. Xu, S. Jachmich, R.R. Weynants and the TEXTOR Team, Plasma Phys. Control. Fusion **47** 1841 (2005)

35 O.E. Garcia, J. Horacek, R.A. Pitts, A.H. Nielsen, W. Fundamenski, J.P. Graves, V. Naulin and J. Juul Rasmussen, Plasma Phys. Control. Fusion **48** L1 (2006)

36 O.E. Garcia, R.A. Pitts, J. Horacek, J. Madsen, V. Naulin, A.H. Nielsen and J. Juul Rasmussen, Plasma Phys. Control. Fusion **49** B47 (2007)

37 J.A. Boedo, J. R. Myra, S. Zweben, R. Maingi, R. J. Maqueda, V. A. Soukhanovskii, J. W. Ahn, J. Canik, N. Crocker, D. A. D'Ippolito, R. Bell, H. Kugel, B. Leblanc, L. A. Roquemore, D. L. Rudakov, and NSTX Team, Phys. Plasmas **21** 042309 (2014)

38 O.E. Garcia, J. Horacek, R.A. Pitts, A.H. Nielsen, W. Fundamenski, V. Naulin and J. Juul Rasmussen, Nucl. Fusion **47** 667 (2007)

39 O.E. Garcia, J. Horacek and R.A. Pitts, Nucl. Fusion **55** 062002 (2015)

40 P. Devynck, J. Brotankova, P. Peleman, M. Spolaore, H. Figueiredo, M. Hron, G. Kirnev, E. Martines, J. Stockel, G. and Van Oost and V. and Weinzettl, Phys. Plasmas **13** 102505 (2006)

41 T.A. Carter, Phys. Plasmas **13** 010701 (2006)

42 A. Theodorsen. O.E. Garcia, J. Horacek, R. Kube and R. A. Pitts, Plasma Phys. Control. Fusion **58** 044006 (2016)

43 G.Y. Antar, S.I. Krasheninnikov, P. Devynck, R.P. Doerner, E.M. Hollmann, J.A. Boedo, S.C. Luckhardt and R.W. Conn, Phys. Rev. Lett **87** 065001 (2001)

44 F. Sattin, N. Vianello and M. Valisa, Phys. Plasmas **11** 5032 (2004)

45 F. Sattin, M. Agostini, P. Scarin, N. Vianello, R. Cavazzana, L. Marrelli, G. Serianni, S.J. Zweben, R.J. Maqueda, Y. Yagi, H. Sakakita, H. Koguchi, S. Kiyama, Y Hirano and J L Terry, Plasma Phys. Control. Fusion **51** 055013 (2009)

46 B. Labit, I. Furno, A. Fasoli, A. Diallo, S.H. Müller, G. Plyushchev, M. Podestà and F.M Poli, Phys. Rev. Lett. **98** 255002 (2007)

47 O.E. Garcia, Phys. Rev. Lett. **108** 265001 (2012), R. Kube and O.E. Garcia, Phys. Plasmas **22** 012502 (2015)

48 O.E. Garcia, S.M. Fritzner, R. Kube, I. Cziegler, B. LaBombard and J.L. Terry, Phys. Plasmas **20** 055901 (2013), O.E. Garcia, I. Cziegler, R. Kube, B. LaBombard and J.L. Terry, J. Nucl.

Mater **S438** S180 (2013)

[49] H.L. Pécseli and J. Trulsen, Phys. Fluids B **1** 1616 (1989)

[50] F.J. Øynes, H.L Pecseli and K. Rypdal, Phys. Rev. Lett **75** 81 (1995)

[51] L.L. Lao, H. St John, R.D. Stambaugh, A.G. Kellman and W. Pfeiffer, Nucl. Fusion **25** 1611 (1985)

[52] N. Smick and B. LaBombard, Rev. Sci. Instruments **80** 023502 (2009)

[53] N. Smick. B. LaBombard and I.H. Hutchinson, Nucl. Fusion **53** 023001 (2013)

[54] R.S. Granetz, I.H. Hutchinson, J. Gerolamo, W. Pina and C. Tsui, Rev. Sci. Instruments **61** 2967 (1990)

[55] I. H. Hutchinson, *Principles of Plasma Diagnostics*, Cambridge University Press (2002)

[56] S.J. Zweben, R.J. Maqueda, J.L. Terry, T. Munsat, J.R. Myra, D. D'Ippolito, D.A. Russell, J.A. Krommes, B. LeBlanc, T. Stoltzfus-Dueck, D.P. Stotler, K.M. Williams, C.E. Bush, R. Maingi, O. Grulke, S.A. Sabbagh and A. E. White, Phys. Plasmas **13** 056114 (2006)

[57] R. Maqueda, D.P. Stotler and the NSTX Team, Nucl. Fusion **50**, 075002 (2010)

[58] M. Agostini, J.L. Terry, P. Scarin and S.J. Zweben, Nucl. Fusion **51** 053020 (2011)

[59] R. Fraile, E. García-Ortega, J. Appl. Meteor. **44** 1620 (2005)

[60] B. LaBombard, J. Goetz, C. Kurz, D. Jablonski, B. Lipschultz, G. McCracken, A. Niemczewski, R.L. Boivin, F. Bombarda, C. Christensen, S. Fairfax, C. Fiore, D. Garnier, M. Graf, S. Golovato, R. Granetz, M. Greenwald, S. Horne, A. Hubbard, I. Hutchinson, J. Irby, J. Kesner, T. Luke, E. Marmar, M. May, P. O'Shea, M. Porkolab, J. Reardon, J. Rice, J. Schachter, J. Snipes, P. Stek, Y. Takase, J.L. Terry, G. Tinios, R. Watterson, B. Welch, and S. Wolfe, Phys. Plasmas **2** 2242 (1995)

[61] J.R. Myra, D.A. D'Ippolito, S.I. Krasheninnikov and G.Q. Yu, Phys. Plasmas **11** 4267 (2004)

[62] B. LaBombard, Phys. Plasmas **9** 1300 (2002)

[63] N. Fedorczak, J.P. Gunn, J.-Y. Pascal, Ph. Ghndrih, Y. Marandet, and P. Monier-Garbet, Phys. Plasmas **19** 072313 (2012)

[64] D. Carralero, G. Birkenmeier, H.W. Müller, P. Manz, P. deMarne, S.H. Müller, F. Reimold, U. Stroth, M. Wischmeier, E. Wolfrum and The ASDEX Upgrade Team, Nucl. Fusion **54** 123005 (2014)